2021 IEEE International Conference on Robotics and Automation (ICRA 2021)
May 31 - June 4, 2021, Xi'an, China

2021 IEEE International Conference on Robotics and Automation (ICRA) | 978-1-7281-9077-8/21/$31.00 ©2021 IEEE | DOI: 10.1109/ICRA48506.2021.9561294

Small Autonomous Robot Actuator (SARA): A Solar-Powered Wireless MEMS Gripper

Alex Moreno[1], Austin Patel[1], Daniel Teal[1], Hani C. Gomez[1], Andrew Fearing[1], Jan S. Rentmeister[2], Jason Stauth[2] and Kristofer Pister[1]

***Abstract*— Solar-powered actuation of a 15 mN electrostatic MEMS gripper was demonstrated while wirelessly triggered by IEEE 802.15.4 RF signals. The solar-powered gripper was shown to actuate at a rate of 640 um/s. The complete system is composed of three capacitors and three chips: MEMS gripper, microprocessor/crystal-free radio, and solar cell array/high voltage buffer. Control signals for the electrostatic inchworm motors originate from the $3\times2\times0.3\,mm^3$ chip with an ARM Cortex-M0 microprocessor and are passed through 119 V high voltage buffers. Power for all components, including the crystal-free radio, microprocessor, and 119 V buffers, is supplied by a multi-output array of solar cells on a CMOS SOI chip under 200 mW/cm^2 irradiation.**

I. INTRODUCTION

One ideal for an autonomous microrobotic system is one composed of motors, mechanisms, sensing, computation, communication, and power, which is able to interact with its environment and the internet in an intelligent manner. Much progress has been made in the development of all of the required components, and in the integration of full systems. We report here a modest level of autonomy in a modular combination of a small number of components, with application to a broader set of microrobots. The motor and mechanism used here is a MEMS gripper described in [1]. The gripper is a single degree-of-freedom actuator, very simple from a robotics perspective. But it is made in a MEMS fabrication process which has been used to fabricate more complicated robot structures, such as jumpers [2] and a twelve degree-of-freedom hexapod [3], as well as a quadthruster ionocraft [4]. The jumper and walker use the same basic electrostatic inchworm motor as the gripper. The high voltage chip used here, Zappy2, was designed to drive this type of motor.

Previous work on untethered systems has shown that small robots are able to accomplish interesting tasks in healthcare and bioengineering [5], and construction [6]. In many cases these untethered robots might benefit from a wireless microgripper attachment, as would some of the autonomous robots below.

There are many small autonomous robot systems in the multiple cubic inch size range [7], [8], [9]. Communication is a key enabler in several of these systems [7], [10]. Indeed, communication may be the only area in which man-made microrobots can outperform their natural counterparts. While

[1]Berkeley Sensor & Actuator Center, Electrical Engineering & Computer Sciences Department, University of California, Berkeley, USA moreno@berkeley.edu

[2]Thayer School of Engineering, Dartmouth College, Hanover, NH, USA

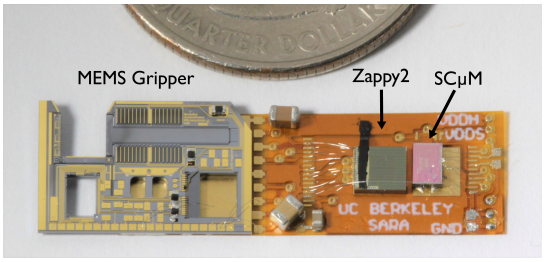

Fig. 1: MEMS Gripper, HV Buffer & Solar Cell Array Chip, Single Chip Micro Mote (left to right). Two SCμM chips are stacked due to initial SCμM malfunctioning. The dimensions of SARA are $9.5\times31.55\,mm^2$

TABLE I: SARA Weight Specifications

Item	Mass (mg)
Empty Flex PCB	71.8
SCμM (Stacked)	8.6
Zappy 2	17.3
MEMS Gripper	137.9
0402 Capacitor (22 μF VDDIO)	3.8
0805 Capacitor (100 μF VBAT)	26.2
0805 Capacitor (100 nF VDDH)	17.2
Solder and wirebonds	3.1
Total Mass	285.9

IR communication is simple and useful for local operations, RF communication allows longer-range, multi-hop mesh networks, and easier integration into existing networks and infrastructure. The Bluetooth chip used by Iyer, et al. [11] allowed them to send images over 120 meters. The radio used by Sabelhaus et al. [7] speaks the 802.15.4 PHY and MAC protocol natively. This protocol is the basis of a highly reliable low power mesh networking communication stack, OpenWSN [12]. The Single Chip micro Mote, SCμM, was designed to perform the computation and communication required by swarms of simple microrobots, and is able to run the OpenWSN stack [13]. It has some features in common with the chip developed by Zhang et al. [14].

There have been several autonomous microrobots in the sub-gram size range, mostly aerial vehicles. The 10 mg robot built by Hollar et al. [15] used inchworm motors and a solar cell array and was able to do autonomous pushups, with a small amount of lateral motion, under roughly one sun of illumination. The controller was a simple CMOS finite state machine, with no sensor feedback. The 300 mg robot built by Churaman et al. [16] was able to jump 11 body lengths when triggered by an on-board light sensor. The logic

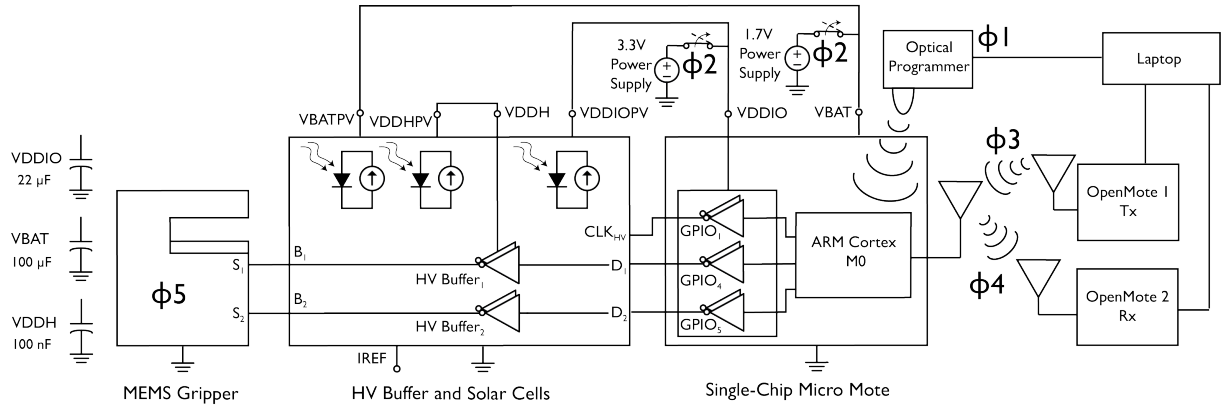

Fig. 2: System block diagram including power domains, phases of operation, and all components.

was hard-wired. James et al. [17] were the first to achieve takeoff, however briefly, of a 190 mg robot under 200 suns of illumination. The 259 mg robot built by Jafferis et al. [18] achieved many body lengths of autonomous flight under only a few suns of illumination. Both of these last two flapping wing robots used open-loop control, but included a digital microcontroller, indicating that future sensor integration will be possible.

Previous work has demonstrated the operation of electrostatic inchworm motors using multi-junction solar cell arrays [19], coupled with an external silicon leg-sweeping mechanism. Bellew et al. [20] demonstrated the integration of solar cells, CMOS, and MEMS into a single process, pointing to a future in which the size, weight, and frustration associated with multi-chip assembly is minimized.

The work described here is a step toward demonstrating standards-compatible mesh-networked swarms of centimeter-scale microrobots.

II. SYSTEM DESCRIPTION

The SARA robot consists of three chips and three capacitors. In addition, two OpenMote B CC2538 IoT devices were used for RF communication between SARA and a laptop, one for sending commands to SCµM and the other for receiving from SCµM [21]. Additionally, a Teensy 3.6 microcontroller with an infrared LED was used to optically program and calibrate the SCµM chip [22]. The block diagram of the system can be seen in Figure 2.

A. The Single Chip µMote (SCµM)

SCµM is a $3\times2\times0.3\,\text{mm}^3$ CMOS SoC featuring an ARM Cortex-M0 microprocessor, BLE transmitter, and a standards-compatible crystal-free 802.15.4 transceiver [23]. The chip also features an ADC, 16 0.8 V-3.6 V GPIOs, and an optical receiver used for optical programming and calibration. SCµM requires only one 1.2 V-1.8 V power supply connected to VBAT to operate [23], but the GPIOs may be driven from a separate supply, VDDIO. For proper interfacing with the high voltage buffers on Zappy2, the solar cell array provides VBAT = 1.8 V and VDDIO = 3.5 V.

TABLE II: SCµM System Clocks

Clock	Purpose
20 MHz RC	Source for Cortex microprocessor
2.4 GHz LC	Dictates radio channel frequency
2 MHz RC	Radio chipping clock
64 MHz RC	Sample RF intermediate frequency
500 kHz RC (derived)	User-defined interrupts

TABLE III: SCµM Operating Current (1.5 V)

State	Approximate Current
5 MHz Clock Rate (Normal)	350 µA
5 MHz Clock Rate (Radio on)	1.6 mA
78 kHz Clock Rate (Low power)	200 µA

By removing the crystal reference, SCµM is able to further reduce size and cost of microrobotic devices. In place of a crystal reference, SCµM uses on-chip CMOS oscillators as detailed in Table II. However, this means that on-chip oscillators need to be calibrated to ensure standards compatible 802.15.4 radio operation. Notably, the 2.4 GHz LC oscillator used to set the local oscillator (LO) at the desired radio channel frequency is configured using three, 5-bit capacitive tuning DACs referred to as the coarse, mid, and fine tuning settings. Other calibrated clocks include the 20 MHz CPU clock, 2 MHz chipping clock, and 64 MHz receiver intermediate frequency sampling clock. Calibration of these clocks has been successfully demonstrated using several different approaches, including an optical programmer [22], temperature-based calibration [24], [25], and RF-based calibration using only packets overheard [26], [27], [28]. The work reported here used the optical programmer.

During normal operation the 20 MHz RC oscillator is divided down to 5 MHz for use as the clock for the Cortex microprocessor. For lower power consumption this oscillator

is divided to 78 kHz. The current consumption at these various operating conditions can be seen in Table III.

B. Zappy2

Zappy2 contains the photovoltaic (PV) arrays that power the robot and high voltage buffers to drive the motors. The $3.26\times3.5\,\mathrm{mm}^2$ chip is fabricated in a 650 V trench-isolated CMOS process and contains more than two hundred PV cells [29]. These PV cells are grouped in series to provide three voltage domains: one to power SCμM (VBATPV; 1.8 V), one as a reference for the SCμM's GPIOs (VDDIOPV; 3.5 V), and one as a high voltage rail to power the electrostatic motors on the MEMS gripper (VDDHPV; 119 V). The performance characteristics of the solar cell arrays are shown in Table IV. Three capacitors of size 100 μF, 22 μF, and 100 nF are used to maintain voltage across VBAT, VDDIO, and VDDH, respectively (Figure 2). In the SARA robot, the lowest allowable successful operating voltages of VBAT, VDDIO and VDDH were measured to be 1.3 V, 3.3 V and 40 V, respectively.

TABLE IV: Solar Output Specifications at $100\,\mathrm{mW/cm}^2$ Irradiation

	VBATPV	VDDIOPV	VDDHPV
V_{OC}	1.8 V	3.5 V	119 V
I_{SC}	280 μA	16 μA	2.4 μA

Zappy2 also contains four high voltage (HV) buffers, two of which are needed to drive a single inchworm motor. These buffers hard switch their outputs between 0 V and VDDHPV at a rate determined by the switching of the input signals. SCμM uses two GPIOs to drive two buffers, and a third GPIO to generate the $\mathrm{CLK_{HV}}$=100 kHz source needed for the Zappy2 internal digital state machine.

Hard switching the HV lines is sub-optimal for electrical to mechanical conversion efficiency, and because it requires significant capacitance on the HV supply to avoid drooping in the supply voltage. Both of these problems can be solved using an improved version of the HV chip [30], but for SARA we simply added a HV capacitor that was large compared to the load capacitance of the electrostatic actuators, roughly 70 pF. 100 nF was overkill.

For this SARA integration, the solar array is provided with $200\,\mathrm{mW/cm}^2$ irradiation to provide VBATPV to SCμM with 560 μA at 1.86 V.

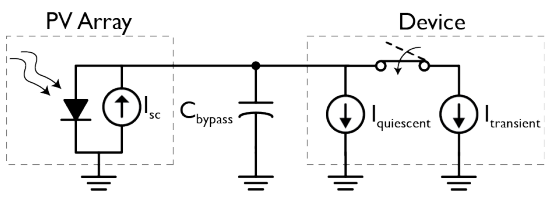

Fig. 3: Model used to maintain proper operating voltages and functionality of SARA. Typically $\mathrm{I_{quiescent}}$=350 μA and $\mathrm{I_{transient}}$=1250 μA during radio operation.

Figure 3 shows a simple model of the VBAT supply and consumption, discussed below.

C. MEMS Gripper

The $14.5\times9.5\times0.6\,\mathrm{mm}^3$ MEMS gripper used in SARA is a later iteration of the design by Schindler et al. [1]. The gripper is microfabricated in a three mask silicon-on-insulator process with a 40 μm thick device layer, and in this silicon device layer is an electrostatic inchworm motor—using the motor architecture proposed in [31]—which linearly actuates the gripper jaw up to 3 mm when suitably powered. The motor consists of a shuttle and two arrays of gap closing actuator finger pairs (with 1536 finger pairs per array). Each of these arrays is a capacitive transducer connected to ground and one high voltage (>40 V) input signal. In this work, the input signals are generated by the SCμM chip and buffered to high voltage by Zappy2. When an input signal is raised to a high voltage, the corresponding array charges, closing its finger pairs, and via a compliant mechanical linkage pushes the shuttle forward 2 μm then holds it in place. If the second array is then charged and the first is released, the shuttle moves an additional 2 μm. Driving the two arrays with >50 % duty cycle square waves 180 degrees out of phase creates continuous movement. When both arrays are discharged simultaneously, the shuttle is free to move and is retracted by a silicon serpentine spring; this is how the gripper jaw returns to its original position.

As with stepper motors, since the motor moves a fixed distance every input signal period, its actuation speed is proportional to the input signal frequency f [31]. In this implementation with $d = 2\mu\mathrm{m/step}$ and $n = 2\,\mathrm{steps/period}$, the motor moves at speed $n{\cdot}d{\cdot}f$: $1\,\mathrm{mm\,s^{-1}}$ at 250 Hz or $4\,\mu\mathrm{m\,s^{-1}}$ at 1 Hz. This gripper has been successfully actuated at speeds up to $1\,\mathrm{mm\,s^{-1}}$ with an external power supply (likely limited by excessive friction in the integrated system) [1]. Experimental tests of the same motor architecture have demonstrated $35\,\mathrm{mm\,s^{-1}}$ movement [32].

Each of the two capacitive transducer arrays has approximately 40 pF maximum (closed) capacitance (and a parasitic 30 pF in parallel for total capacitance $C \approx 70\mathrm{pF}$). When its input signal is raised high, the array charges with energy $\frac{1}{2}CV^2$ and puts an additional $\frac{1}{2}CV^2$ toward mechanical work and heat. When the signal is returned to ground the stored capacitive energy is lost. Thus the power draw of the entire motor on the drive electronics is approximately $2{\cdot}\frac{1}{2}CV^2{\cdot}n{\cdot}f$, e.g., 0.35 mW at $1\,\mathrm{mm\,s^{-1}}$ and 100 V, or 56 μW at $1\,\mathrm{mm\,s^{-1}}$ and 40 V. Note that at zero speed, i.e., holding position without movement, the motor theoretically draws negligible power. In reality, leakage current due to parasitics, especially parallel resistance when the array fingers are closed, can dominate; we explore this in later sections (see Figure 8). The advantage of higher voltage is that the motor force is proportional to voltage squared: this motor, after inefficiencies, provides up to 15 mN at 100 V or 2.4 mN at 40 V [1]. Motor efficiency as defined by [31] is $\eta \approx 15\mathrm{mN}{\cdot}2\mu\mathrm{m}/\frac{1}{2}CV^2 \approx 9\%$ (and parasitics—see Figure 8—reduce this further). This could be increased significantly by

using a variable-voltage driving waveform to reduce both nonlinearities in the capacitive transducer and RC charging losses [31], [30].

III. SYSTEM OPERATION

The integrated SARA microsystem operates in 5 phases indicated in Figure 2 and detailed in this section.

A. Phase $\phi 1$: Optically Program and Calibrate

A Teensy 3.6 microcontroller with an IR LED is used to send signals to the optical receiver on SCμM in order to bootload a program [22]. After programming, SCμM enters an optical calibration phase. This calibration is needed to calibrate the CMOS oscillators on SCμM since the chip lacks a crystal reference. The same IR programmer sends 20 pulses of an optical signal at 10 Hz to trigger optical interrupts on SCμM [22]. Upon receiving an interrupt, SCμM uses the time between interrupts as an absolute reference for calibrating its oscillators. The calibrated clocks include a 20 MHz HF CPU clock, a 2 MHz RC chipping clock, and an IF radio clock.

During bootup, SCμM has the following VBAT current transient: 300 μA unprogrammed/idle, 350 μA for 0.5 s while programming and initializing, 1.6 mA optical calibration for 2 s, and lastly idle at 350 μA. The 1.6 mA exceeds the 560 μA provided by the solar cells at 200 mW/cm^2. Thus, while calibrating, SCμM is connected to an external 1.7 V VBAT. Additionally, an external 3.3 V VDDIO source is connected during calibration to ensure that the Zappy2 FSM is properly initialized.

B. Phase $\phi 2$: Disconnect Power Supply and Calibrate LC

Once calibrated, the external 1.7 V and 3.3 V power sources are disconnected and SCμM operates autonomously on solar power from Zappy2. Under 200 mW/cm^2 irradiation (2 suns) provided by a fiber optic light illuminator, the solar cells provide 560 μA at 1.86 V. This provides power to operate SCμM at a reduced 78 kHz clock rate (I_{VBAT}=200 μA) between periods of full speed operation at 5 MHz (I_{VBAT}=350 μA). The 2 suns illumination was chosen as the 560 μA current provided exceeds the I_{VBAT}=350 μA idle current. Additionally, it provides enough current along with the 100 μF VBAT capacitor to operate SCμM with radio-on I_{VBAT}=1.6 mA for ~2 ms periods while still maintaining 802.15.4 standard compatibility. Further justification is provided in section III-C.

Additional calibration is required to set the radio local oscillator frequency to properly transmit 802.15.4 packets at 2.405 GHz for channel 11 as well as receive packets at 2.410 GHz on 802.15.4 channel 12. This additional calibration is needed as the optical programming phase is not accurate enough to calibrate the local oscillator. To calibrate, SCμM sweeps across tuning settings for each of the three 5-bit capacitive DACs used to set the frequency for the LC local oscillator (coarse, mid, and fine settings). The LC codes are swept until a packet is properly transmitted on channel 11 to an RX OpenMote. Next, the LC codes are again swept until SCμM properly receives a packet on channel 12 from an TX OpenMote (Figure 2). The TX and RX LC configuration codes are then fixed and SCμM is now properly calibrated to transmit and receive.

The LC is calibrated with the goal of maintaining 802.15.4 standard compatibility. This standard defines a ±40 ppm maximum local oscillator frequency error which is difficult to achieve without a crystal reference. This is especially challenging in an energy-constrained and solar-powered system due to large voltage drops across the 100 μF VBAT capacitor that occur during radio operation which shift the frequencies of the CMOS oscillators (see section III-C).

Furthermore, this calibration is complicated by the 160 ppm/°C [33] and −40 ppm/°C [23] temperature dependence of the 2 MHz radio chipping clock and 2.4 GHz radio local oscillator, respectively.

In prior work, SCμM and Zappy2 have been integrated into a wireless temperature sensing node featuring temperature based LC compensation across a temperature range of 35.5 °C to 40.0 °C [25]. For this integration the LC codes are fixed as previously described rather than continuously calibrated. Future work could integrate this continuous LC calibration into the SARA robot.

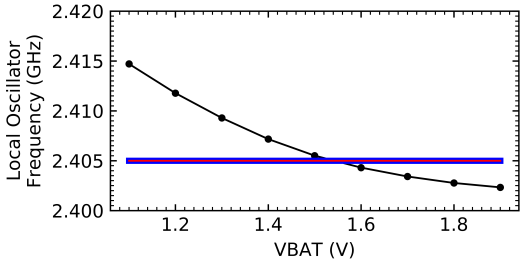

Fig. 4: Crystal-free radio local oscillator frequency vs. VBAT voltage at a fixed LC tuning setting. Red line shows ±40 ppm tolerance band of 802.15.4 standard and blue line shows ±150 ppm tolerance of OpenMote.

C. Phase $\phi 3$: Receive Wireless Command

While operating, the radio is enabled for 1 ms to attempt to receive an 802.15.4 packet from a TX OpenMote (Figure 2). This requires 1.6 μC of charge for I_{radio_on}=1.6 mA. The transient current of SCμM during radio operation under solar power can be seen in Figure 5. The 1 ms radio on period was chosen to minimize voltage drop on VBAT while the radio is on. The TX OpenMote is continuously transmitting 6 byte packets with a command to actuate the gripper. Phase $\phi 3$ is repeated until a command is received.

With the solar cell array under 200 mW/cm^2 irradiation and the 100 μF bypass capacitor across VBATPV, SCμM receives 560 μA at 1.86 V. This can power SCμM at I_{radio_on} of 1.6 mA for 25 ms before VBAT drops from 1.86 V to the operating minimum of 1.3 V. Additionally, SCμM has been shown to send and receive packets under solar with a 20 μF capacitor which can keep the radio on for 11 ms.

In practice, however, such a large voltage drop across VBAT shifts the local oscillator frequency and prevents

proper radio operation (Figure 4). The slope of the LO frequency vs. VBAT curve (Figure 4) at VBAT=1.8 V is approximately 5 MHz V^{-1}. To maintain ±40 ppm stability (±100 kHz), the VBAT supply must be stable to less than ±20 mV variation. A 20 mV VBAT drop limit permits the radio to be enabled for at most 1.92 ms to maintain standards compatibility.

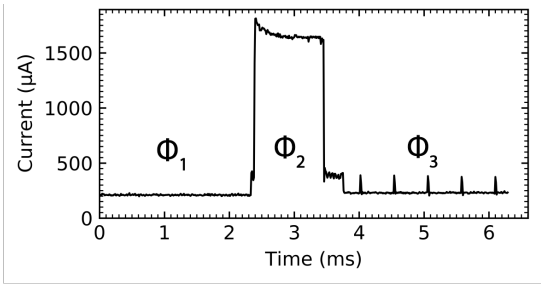

Fig. 5: VBAT current during wireless 802.15.4 receive (200 mW/cm^2 irradiation; 47 µF VBAT bypass capacitor). ϕ_1: Low power (F_{cortex}=78 kHz), ϕ_2: RX with radio on, ϕ_3: periodic wake up to F_{cortex}=5 MHz

D. Phase ϕ4: Send Acknowledgement

After receiving a command to close the gripper, SCµM enables its radio for 4 ms to transmit a 10 byte packet to an OpenMote to confirm that the command was received. The current consumption during the 4 ms transmission period is presented in Figure 7. Transmitting packets is difficult due to high radio-on current draw which causes a drop in VBAT voltage as charge is pulled from the 100 µF VBAT bypass capacitor. The challenges of maintaining the proper local oscillator frequency are similar to those described in section III-C, but now the radio is on for a longer period of time (4 ms TX vs. 1 ms RX). Despite this increased radio on period, SCµM was able to properly send packets as the transmission completes within the first 1 ms (corresponds to ~40 mV VBAT drop; see Figure 6). Further development has decreased the total radio on time to 1 ms. The OpenMote device used for these tests has a higher ±150 ppm frequency tolerance [33] over the ±40 ppm tolerance in the 802.15.4 standard. This increased tolerance was leveraged to help receive packets from SCµM.

E. Phase ϕ5: Actuate Gripper

After sending the acknowledgement that the command to close the gripper was received, SCµM begins sending three control signals through GPIO pins 1, 4, and 5 (powered by VDDIOPV) to Zappy2 (Figure 2). The GPIO output specifications can be seen in Table V. The first signal originates from the SCµM 500 kHz RF timer and is passed through GPIO 1 (Figure 2) as the CLK_{HV} clock source for the Zappy2 digital state machine. GPIO pins 4 and 5 are fed into two of the four high voltage (HV) buffers on Zappy2, which in turn connect the gripper to the Zappy2 VDDHPV HV source. Toggling these pins from 0 V to 3.5 V (with a 60 % duty cycle) and 180 degrees out of phase with each other

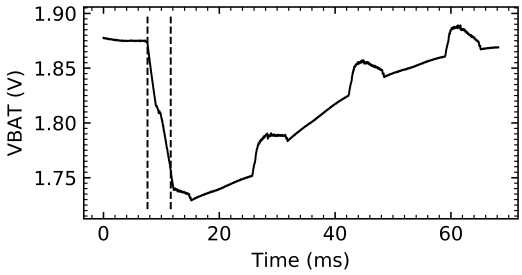

Fig. 6: VBAT voltage vs. time during wireless 802.15.4 transmit (200 mW/cm^2 irradiation; 100 µF bypass capacitor). The dashed lines indicate the 4 ms period when the radio was enabled.

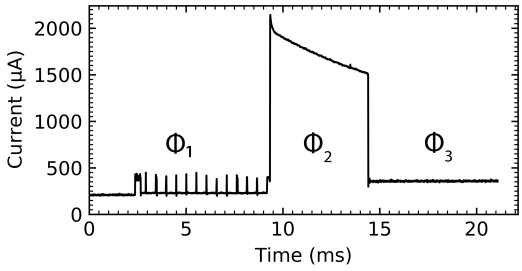

Fig. 7: VBAT current during wireless 802.15.4 transmit (200 mW/cm^2 irradiation; 20 µF bypass capacitor). Phases: ϕ_1: F_{cortex}=78 kHz low power mode and UART logging before transmit, ϕ_2: Transmit 10 byte packet, ϕ_3: F_{cortex}=5 MHz idle state

actuates the electrostatic inchworm motor of the gripper as described in section II-C.

TABLE V: $GPIO_{output}$ Specifications

Specification	Value
VDDIO	0.8-3.6 V
VDDAUX	0.8-1.2 V
F_{max} @ HCLK = 10 MHz	734.25 KHz
$I_{VDDIOleakage}$ @ VDDIO = 3.3 V	4.37 nA
$I_{sink/source}$ @ VDDIO = 3.3 V	19 mA

The current provided by the VDDHPV source on the solar cell and the current consumption of the gripper while held at a DC voltage can be seen in Figure 8. The GPIO signals and the corresponding buffered HV signals used for gripper actuation can be seen in Figure 9.

We can use Figure 8 to determine the maximum speed operating points of the gripper. Because the gripper is capacitive, its speed, as in section II-C, is determined solely by its driving frequency while it charges to the maximum voltage (and thus force) available. At fast speeds, however, insufficient power is supplied to charge the gripper each signal period so the voltage across its capacitance decreases. Once the voltage falls below the minimum 40 V, the gripper fails to move. In this implementation, however, the gripper also has non-negligible leakage current draw under DC input. This sets the minimum power draw of the gripper at a

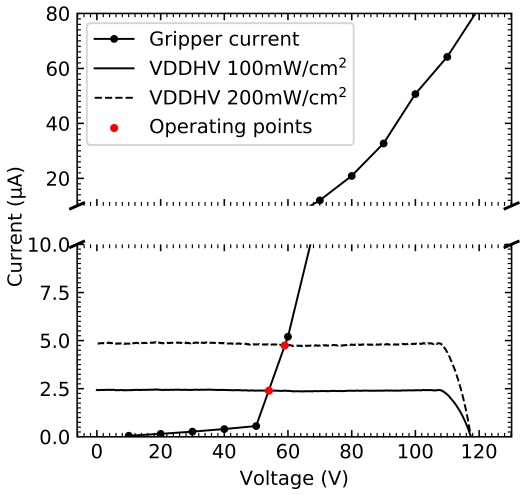

Fig. 8: Measured gripper leakage current under DC supply vs. HV buffer DC voltage, and Zappy2 VDDHPV supply current vs. VDDHPV voltage under 100 mW/cm^2 (measured) and 200 mW/cm^2 irradiation (estimated). Red intersections represent operating points of the system at 100 mW/cm^2 and 200 mW/cm^2 irradiation while closing the gripper at very slow speeds approaching zero and duty cycles approaching 100 %.

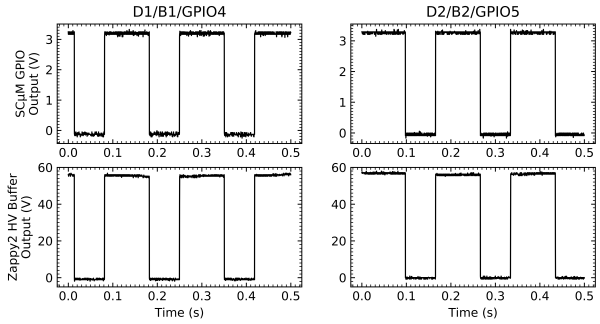

Fig. 9: Toggling of HV buffers driving MEMS gripper at 200 mW/cm^2 irradiation. SCµM GPIO pins 4 and 5 are enabling/disabling 59 V HV buffered outputs D1 and D2 (respectively) on Zappy2. GPIOs toggling at 5.9 Hz with a 60 % duty cycle at a 180 degree phase offset from each other.

given voltage as its speed approaches zero and duty cycle approaches 100%.

Thus, under 200 mW/cm^2 irradiation, the operating point of the HV buffers and the gripper (for slow speeds and high duty cycles) is ~4.75 µA at ~59 V (Figure 8). According to section II-C, at this voltage, the force of the gripper is approximately 5.2 mN. If we assume the leakage current graphed in Figure 8 only appears across the gripper when a motor array is charged (i.e., the gap closing actuators are closed, which makes sense if their fingers are touching and causing a high-resistance short), then the proportion remaining power available to actuate the gripper is 1 minus the duty cycle (here, 60%), for $4.75\mu A{\cdot}59V{\cdot}0.4 = 0.11mW$, which is sufficient for up to 920 µm s^{-1} speed. While testing the integrated SARA system at 200 mW/cm^2 irradiation, GPIO toggling speeds up to 160 Hz resulted in movement, corresponding to a maximum speed of 640 µm s^{-1} closing the full 3 mm distance under solar power in ~4.7 s (the slower-than-theoretical maximum achievable speed implies some of the gripper leakage is always present, reducing power available for movement, and friction may also play a role).

Each of the three Zappy2 voltage domains (VBATPV, VDDIOPV, and VDDHPV) must maintain a minimum voltage during actuation of the MEMS gripper. During gripper actuation, SCµM operates at a F_{cortex}=78 MHz with I_{VBAT}=200 µA. This is within the 560 µA provided by the VBATPV supply. The I_{VDDIO}¡1 µA consumed while toggling the GPIO pins at 160 Hz is well under the ~32 µA provided by the VDDIOPV source. Lastly, the VDDHPV current while toggling and actuating the gripper is on average ~4.75 µA, smoothed by a 100 nF capacitor.

Finally, SCµM returns to Phase ϕ3 and begins listening for packets with actuate gripper commands. The gripper has been demonstrated to repeatedly open and close after multiple iterations of the receive-acknowledge-actuate loop.

IV. CONCLUSION

Under conditions of steady 200 mW/cm^2 irradiation on Zappy2 we have demonstrated full SARA system operation. This includes receiving a six byte wireless command to actuate the gripper from a standard 2.4 GHz 802.15.4 transmitter, transmitting a ten byte standards-compatible 802.15.4 packet as an acknowledgement, and autonomous microprocessor-controlled MEMS gripper actuation. The gripper has then been demonstrated to fully close at a rate of 640 µm s^{-1} to close the full 3 mm distance in roughly 4.7 s. After the gripper has closed the SARA system successfully repeated the entire receive-acknowledge-actuate procedure repeatedly without failure.

The integrated SARA microsystem with power, control, and mechanical elements provides capabilities that previously would not be possible. An autonomous MEMS gripper could be used in micro assembly and manufacturing systems that require manipulation at a µm scale. Feedback control could be obtained by using the contact sensor on the MEMS gripper which could enable a µm scale caliper device to make size measurements of objects. Further developments will allow the integration of new jumping [34], walking [35], and fiber crawling [36] MEMS devices. For example, a MEMS inchworm motor could pull the SARA microsystem along a cord strung across an interior space to use SCµM as an autonomous, battery-free sensor. Multiple devices with SCµM and MEMS chips integrated could also be used in mesh networking systems for micro-scale robotic exploration.

ACKNOWLEDGMENT

This work was supported by the National Science Foundation Graduate Research Fellowship Program under Grant No. DGE 1752814. Any opinions, findings, and conclusions or recommendations expressed in this material are those of the authors and do not necessarily reflect the views of the National Science Foundation.

REFERENCES

[1] C. Schindler, H. Gomez, D. Acker-James, D. Teal, W. Li, and K. Pister, "15 millinewton force, 1 millimeter displacement, low-power MEMS gripper," in *IEEE MEMS*, 2020.

[2] C. B. Schindler, J. T. Greenspun, H. C. Gomez, and K. S. Pister, "A jumping silicon microrobot with electrostatic inchworm motors and energy storing substrate springs," in *2019 20th International Conference on Solid-State Sensors, Actuators and Microsystems & Eurosensors XXXIII (TRANSDUCERS & EUROSENSORS XXXIII)*. IEEE, 2019, pp. 88–91.

[3] D. S. Contreras and K. Pister, "A six-legged MEMS silicon robot using multichip assembly," in *Solid State Sensors and Actuators Workshop, Hilton Head*, 2018.

[4] D. S. Drew, N. O. Lambert, C. B. Schindler, and K. S. Pister, "Toward controlled flight of the ionocraft: a flying microrobot using electrohydrodynamic thrust with onboard sensing and no moving parts," *IEEE Robotics and Automation Letters*, vol. 3, no. 4, pp. 2807–2813, 2018.

[5] M. Sitti, H. Ceylan, W. Hu, J. Giltinan, M. Turan, S. Yim, and E. Diller, "Biomedical applications of untethered mobile milli/microrobots," *Proceedings of the IEEE*, vol. 103, no. 2, pp. 205–224, 2015.

[6] A. Hsu, A. Wong-Foy, B. McCoy, C. Cowan, J. Marlow, B. Chavez, T. Kobayashi, D. Shockey, and R. Pelrine, "Application of micro-robots for building carbon fiber trusses," in *2016 international conference on manipulation, automation and robotics at small scales (MARSS)*. IEEE, 2016, pp. 1–6.

[7] A. P. Sabelhaus, D. Mirsky, L. M. Hill, N. C. Martins, and S. Bergbreiter, "Tinyterp: A tiny terrestrial robotic platform with modular sensing," in *2013 IEEE International Conference on Robotics and Automation*. IEEE, 2013, pp. 2600–2605.

[8] M. Rubenstein, C. Ahler, N. Hoff, A. Cabrera, and R. Nagpal, "Kilobot: A low cost robot with scalable operations designed for collective behaviors," *Robotics and Autonomous Systems*, vol. 62, no. 7, pp. 966–975, 2014.

[9] G. Caprari and R. Siegwart, "Mobile micro-robots ready to use: Alice," in *2005 IEEE/RSJ international conference on intelligent robots and systems*. IEEE, 2005, pp. 3295–3300.

[10] N. Correll, S. Rutishauser, and A. Martinoli, "Comparing coordination schemes for miniature robotic swarms: A case study in boundary coverage of regular structures," in *Experimental Robotics*. Springer, 2008, pp. 471–480.

[11] V. Iyer, A. Najafi, J. James, S. Fuller, and S. Gollakota, "Wireless steerable vision for live insects and insect-scale robots," *Science robotics*, vol. 5, no. 44, 2020.

[12] T. Watteyne, X. Vilajosana, B. Kerkez, F. Chraim, K. Weekly, Q. Wang, S. Glaser, and K. Pister, "Openwsn: a standards-based low-power wireless development environment," *Transactions on Emerging Telecommunications Technologies*, vol. 23, no. 5, pp. 480–493, 2012.

[13] T. Chang, T. Watteyne, B. Wheeler, F. Maksimovic, O. Khan, S. Mesri, L. Lee, I. Suciu, X. Vilajosana, and K. Pister, "6TiSCH on SCμM:running a synchronized protocol stack without crystals," in *ACM Embedded Wireless Systems and Networks*, 2020.

[14] X. Zhang, M. Lok, T. Tong, S. K. Lee, B. Reagen, S. Chaput, P.-E. J. Duhamel, R. J. Wood, D. Brooks, and G.-Y. Wei, "A fully integrated battery-powered system-on-chip in 40-nm cmos for closed-loop control of insect-scale pico-aerial vehicle," *IEEE Journal of Solid-State Circuits*, vol. 52, no. 9, pp. 2374–2387, 2017.

[15] S. Hollar, A. Flynn, C. Bellew, and K. S. J. Pister, "Solar powered 10 mg silicon robot," in *The Sixteenth Annual International Conference on Micro Electro Mechanical Systems, 2003. MEMS-03 Kyoto. IEEE*, 2003, pp. 706–711.

[16] W. Churaman, L. Currano, C. Morris, J. Rajkowski, and S. Bergbreiter, "The first launch of an autonomous thrust-driven microrobot using nanoporous energetic silicon," *Microelectromechanical Systems, Journal of*, vol. 21, pp. 198–205, 02 2012.

[17] J. James, V. Iyer, Y. Chukewad, S. Gollakota, and S. B. Fuller, "Liftoff of a 190 mg laser-powered aerial vehicle: The lightest wireless robot to fly," in *2018 IEEE International Conference on Robotics and Automation (ICRA)*, 2018, pp. 3587–3594.

[18] N. Jafferis, E. Helbling, M. Karpelson, and R. Wood, "Untethered flight of an insect-sized flapping-wing microscale aerial vehicle," *Nature*, vol. 570, pp. 491–495, 06 2019.

[19] K. Saito, D. S. Contreras, Y. Takeshiro, Y. Okamoto, S. Hirao, Y. Nakata, T. Tanaka, S. Kawamura, M. Kaneko, F. Uchikoba *et al.*, "Study on electrostatic inchworm motor device for a heterogeneous integrated microrobot system," *Transactions of The Japan Institute of Electronics Packaging*, vol. 12, pp. E18–009, 2019.

[20] C. L. Bellew, S. Hollar, and K. Pister, "An soi process for fabrication of solar cells, transistors and electrostatic actuators," in *TRANSDUCERS'03. 12th International Conference on Solid-State Sensors, Actuators and Microsystems. Digest of Technical Papers (Cat. No. 03TH8664)*, vol. 2. IEEE, 2003, pp. 1075–1078.

[21] X. Vilajosana, P. Tuset, T. Watteyne, and K. Pister, "OpenMote: Open-Source Prototyping Platform for the Industrial IoT," in *International Conference on Ad Hoc Networks (AdHocNets)*, San Remo, Italy, Sep. 2015, pp. 211–222.

[22] B. Wheeler, A. Ng, B. Kilberg, F. Maksimovic, and K. Pister, "A low-power optical receiver for contact-free programming and 3D localization of autonomous microsystems," in *IEEE UEMCON*, 2019.

[23] F. Maksimovic, B. Wheeler, D. C. Burnett, O. Khan, S. Mesri, I. Suciu, L. Lee, A. Moreno, A. Sundararajan, B. Zhou *et al.*, "A crystal-free single-chip micro mote with integrated 802.15.4 compatible transceiver, sub-mW BLE compatible beacon transmitter, and Cortex M0," in *VLSI 2019*. IEEE, 2019.

[24] T. Yuan, F. Maksimovic, D. C. Burnett, B. Wheeler, L. Lee, and K. S. J. Pister, "Temperature calibration on a crystal-free mote," in *2020 IEEE 6th World Forum on Internet of Things (WF-IoT)*, 2020, pp. 1–5.

[25] A. Moreno, A. Patel, T. Yuan, A. Fearing, J. S. Rentmeister, J. Stauth, and K. Pister, "Solar-powered crystal-free 802.15.4 wireless temperature sensor," in *2020 IEEE Sensors*. IEEE, 2020, pp. 1–4.

[26] I. Suciu, F. Maksimovic, B. Wheeler, D. C. Burnett, O. Khan, T. Watteyne, X. Vilajosana, and K. S. Pister, "Dynamic channel calibration on a crystal-free mote-on-a-chip," *IEEE Access*, vol. 7, pp. 120 884–120 900, 2019.

[27] I. Suciu, F. Maksimovic, D. Burnett, O. Khan, B. Wheeler, A. Sundararajan, T. Watteyne, X. Vilajosana, and K. Pister, "Experimental clock calibration on a crystal-free mote-on-a-chip," in *IEEE INFOCOM 2019-IEEE Conference on Computer Communications Workshops (INFOCOM WKSHPS)*. IEEE, 2019, pp. 608–613.

[28] T. Chang, T. Watteyne, F. Maksimovic, B. Wheeler, D. C. Burnett, T. Yuan, X. Vilajosana, and K. S. J. Pister, "Quickcal: Assisted calibration for crystal-free micromotes," *IEEE Internet of Things Journal*, vol. 8, no. 3, pp. 1846–1858, 2021.

[29] J. S. Rentmeister, M. H. Kiani, K. S. Pister, and J. T. Stauth, "A 120-330V, sub-μa, 4-channel driver for microrobotic actuators with wireless- optical power delivery and over 99% current efficiency," in *2020 IEEE Symposium on VLSI Circuits*, Honolulu, HI, USA, 2020.

[30] Y. Li, B. L. Dobbins, and J. T. Stauth, "An optically powered, high-voltage, switched-capacitor drive circuit for microrobotics," *IEEE Journal of Solid-State Circuits*, 2020.

[31] I. Penskiy and S. Bergbreiter, "Optimized electrostatic inchworm motors using a flexible driving arm," *Journal of Micromechanics and Microengineering*, vol. 23, no. 1, p. 015018, Dec. 2012, publisher: IOP Publishing.

[32] D. S. Contreras and K. S. J. Pister, "Dynamics of electrostatic inchworm motors for silicon microrobots," in *2017 International Conference on Manipulation, Automation and Robotics at Small Scales (MARSS)*, Jul. 2017, pp. 1–6.

[33] B. Wheeler, "Low power, crystal-free design for monolithic receivers," Ph.D. dissertation, EECS Department, University of California, Berkeley, May 2019.

[34] C. B. Schindler, J. T. Greenspun, H. C. Gomez, and K. S. J. Pister, "A jumping silicon microrobot with electrostatic inchworm motors and energy storing substrate springs," in *2019 20th International Conference on Solid-State Sensors, Actuators and Microsystems Eurosensors XXXIII (TRANSDUCERS EUROSENSORS XXXIII)*, 2019, pp. 88–91.

[35] D. S. Contreras, D. S. Drew, and K. S. J. Pister, "First steps of a millimeter-scale walking silicon robot," in *2017 19th International Conference on Solid-State Sensors, Actuators and Microsystems (TRANSDUCERS)*, 2017, pp. 910–913.

[36] R. S. Zoll, C. B. Schindler, T. L. Massey, D. S. Drew, M. M. Maharbiz, and K. S. J. Pister, "Mems-actuated carbon fiber microelectrode for neural recording," *IEEE Transactions on NanoBioscience*, vol. 18, no. 2, pp. 234–239, 2019.